

# Learning to Jointly Deblur, Demosaick and Denoise Raw Images

Thomas Eboli<sup>\*,†</sup>

Jian Sun<sup>‡</sup>

Jean Ponce<sup>\*,†</sup>

November 14, 2021

## Abstract

We address the problem of non-blind deblurring and demosaicking of noisy raw images. We adapt an existing learning-based approach to RGB image deblurring to handle raw images by introducing a new interpretable module that jointly demosaicks and deblurs them. We train this model on RGB images converted into raw ones following a realistic invertible camera pipeline. We demonstrate the effectiveness of this model over two-stage approaches stacking demosaicking and deblurring modules on quantitative benchmarks. We also apply our approach to remove a camera’s inherent blur (its color-dependent point-spread function) from real images, in essence deblurring sharp images.

## 1 Introduction

The goal of this work is to deblur, denoise and demosaick raw images. Raw data is important since it captures the most direct information we have about the observed scene, before any digital post-processing such as color transformations and gamma correction [3]. An important application is the removal of the optical aberrations introduced by the lens point-spread function (PSF). Indeed, any photograph, even perfectly focused and in the absence of any motion, contains some blur caused by its optics, ranging from geometric distortions to chromatic aberrations [28, 34]. Removing these artifacts is a (little explored) instance of joint image demosaicking and non-blind deblurring addressed in this presentation.

Most approaches to image deblurring focus on sophisticated priors [15, 37], convolutional neural networks (CNNs) [21, 32], or a combination of both [4, 6, 16, 35]. Recent algorithms are robust to various noise levels [16], large [6, 35] and even approximate kernels [22], but they often ignore several stages of the camera pipeline connecting the analog image in the focal plane to the digital blurry image recorded by the camera.

Blur is caused by various, color-dependent optical phenomena [28, 34], camera and/or scene motion, and spatial, spectral and temporal integration over the pixel area. In particular, a single grey value is typically recorded at each pixel according to the Bayer pattern to form the final *raw* image.

Raw images are interpolated with filtering techniques [18, 20] or learning-based approaches [9, 14] into linear RGB (aka linRGB) images [3, 24]. This *demosaicking* operation is often highly non-linear. Sensor noise follows a statistical model whose parameters are estimated empirically from raw images [7] or learnt with a neural network on a corpus of image pairs [1], which is much more realistic than a Gaussian model. LinRGB images are finally converted into the standard RGB (aka sRGB) format through an image signal processing (ISP) pipeline [3].

This complex process suggests that the classical model of convolving a sharp image with a linear filter to form its blurry version can be improved to better fit real digital cameras. We thus start from a raw, blurry and noisy image to predict a sharp and denoised linRGB image. We use a realistic image formation model, embed it into a penalized energy term, and unroll a few stages of an iterative solver within a parametric function inspired by [35] and trained with samples preprocessed with a modified variant of the linRGB-to-sRGB conversion pipeline from [3]. We finally apply this model to optical aberrations removal from images taken with high-end cameras whose PSF has been estimated separately.

Our main contributions can be summarized as follows:

- We introduce a joint deblurring, demosaicking and denoising formulation motivated by a realistic camera pipeline;

<sup>\*</sup>INRIA.

<sup>†</sup>Département d’informatique de l’ENS, Ecole normale supérieure, CNRS, PSL Research University, France.

<sup>‡</sup>Department of Information Science, School of Mathematics and Statistics, Xi’an Jiaotong University, P.R.China.

✉: Correspondance at [thomas.eboli@inria.fr](mailto:thomas.eboli@inria.fr)

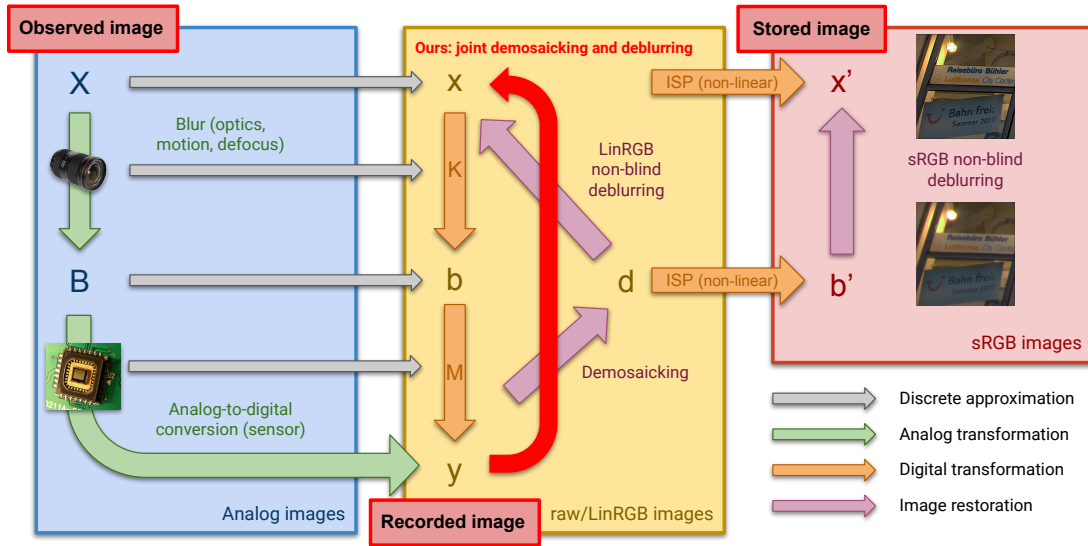


Figure 1: Starting from an observed image  $X$  in its focal plane, a digital camera records a blurry, mosaicked and noisy raw image  $y$ . Several processing stages are required to display a sharp sRGB image  $x'$ . We predict from  $y$  a sharp linRGB image  $x$ , which consists in inverting the linear operator  $MK$ . We do not need an intermediate demosaicked image  $d$  that might contain prediction errors, Moiré artifacts and smoothed details. The image  $x$  is further converted into sRGB format with an ISP pipeline.

- a penalized energy based on this forward model optimized with a splitting method. We unroll a few stages of this iterative solver within a parametric function trained on blurry, mosaicked and noisy images generated with [3];
- we present an experimental comparison with two-stage methods demonstrating the benefits of our approach and;
- we present an application of the proposed model to the removal of blur and chromatic aberrations caused by a camera's PSF on both synthetic and real images.

## 2 Related work

**ISP pipeline models.** Previous approaches for modelling realistic image noise have focused on estimating an empirical noise distribution in linRGB and raw images. Foi *et al.*, [7] model noise as a Poissonian-Gaussian mixture model, also used in [2, 24] for generating realistic images. Since noise is better modelled on raw/linRGB images, several approaches for image denoising directly work on mosaicked raw images, yielding joint demosaicking and denoising methods [9, 12–14]. In particular, [12, 13] predict denoised and demosaicked linRGB images but compute the training error on its sRGB versions since images are ultimately rendered in this color format. Such supervision for CNNs demands large corpuses of aligned image pairs that are hard to obtain in general for image restoration tasks. Brooks *et al.*, [3] simulate a forward model approximating a general ISP pipeline for generating raw/linRGB degraded images from sRGB clean ones. It is made invertible such that supervision of CNNs predicting linRGB/raw images with sRGB targets is possible. Likewise, Nah *et al.*, [21] invert gamma correction to build blurry training data but most deblurring approaches only tackle sRGB images.

**Image deblurring.** Classical approaches to deconvolution (aka non-blind deblurring) include Wiener filtering [10] and variational methods [15, 37] built with handcrafted or learnt priors on image gradients and patches. Optimization is traditionally carried out with a technique such as half-quadratic splitting (HQS) [8]. HQS has become the backbone of parametric functions unrolling a few iterations to build interpretable methods with learnable priors [6, 16, 26, 35]. Another trend [5, 27] is to learn a CNN that compensates the ringing artifacts of Wiener filtering. Finally, some methods [21, 32] give up the need

for an image forward model by training highly-engineered architectures with large collections of blurry and sharp images as supervision for blind image deblurring.

**Joint deblurring and demosaicking.** A classical approach to this problem is to combine demosaicking and a non-blind deblurring approaches into a two-stage model [28]. Joint demosaicking and deblurring can also be modelled as solving an inverse problem with edge-preserving priors and spectral regularization [30, 33]. Liang *et al.*, [19] synthesize training pairs composed of blurry raw and sharp sRGB images from videos taken with a GoPro camera and train a multi-branch CNN to address joint blind deblurring and demosaicking. Such data is hard to collect and lacks diversity because of the small number of different scenes recorded. We instead use the ISP pipeline [3] to synthesize an unlimited number of blurry and noisy raw images.

### 3 Image formation model

#### 3.1 Camera pipeline

The overall image acquisition pipeline is summarized in Figure 1. On our model, we start from an idealized, sharp and wavelength-dependent irradiance function  $X$  defined over the continuous image domain. The optics of the camera transform it into a blurry function  $B$ , which is then digitized into a raw image  $y$  with spatial, temporal and spectral integration processes corresponding to the pixel extent, the exposure time (including motion blur), and the Bayer pattern typically used in digital cameras. The raw image is then a *demosaicked* linRGB image  $d$  interpolating the missing color channels (see, for example, [18]), before being converted through the ISP pipeline into an sRGB image  $b'$ . It is impossible to recover the continuous-domain function  $X$  from discrete measurement. We thus estimate instead a sharp digital  $x$  mapping onto  $y$  through an approximation of the actual image formation process.

#### 3.2 Approximate forward model

In Figure 1, the matrices  $K$  and  $M$  approximate respectively the blur caused by the optics, motion and defocus for the former, and the sampling of colors in the RGB blurry image by the sensor in the latter. The approximate forward model represented in the yellow box of Figure 1 thus reads

$$y = MKx + \varepsilon \quad \text{with} \quad \varepsilon \sim \mathcal{N}(0, \lambda_s MKx + \lambda_r), \quad (1)$$

where, according to [3, 7], the vector  $\varepsilon$  is the sensor’s noise seen on a raw or linRGB image can be modelled as a pixel-varying zero-mean Gaussian distribution with variance  $\lambda_s MKx + \lambda_r$ . It linearly depends on  $MKx$  and two scalars: a scaling weight  $\lambda_s$  and an offset  $\lambda_r$  representing respectively the impact of shot and read noise [7].

This model contrasts with classical approaches for non-blind deblurring [4, 6, 16, 35, 37] simply considering a blur matrix  $K$  between the sharp and blurry sRGB images  $x'$  and  $b'$  in the red box of Figure 1, stored on a device.

The traditional forward model for image deblurring assumes that the known blurry sRGB image  $b'$  has been obtained by applying a linear operation, *e.g.*, the convolution with a linear blur kernel, to an unknown sharp sRGB image  $x'$ . However this approach is a simplification of the physical model causing blur on the analog image  $B$  and thus ignores the different, possibly non-linear, components and transformations in a camera and shown in Figure 1. A linear forward model linking blurry and sharp images such as (1) is thus only valid between linRGB images. Nah *et al.*, [21] indeed restore linRGB blurry images but they assume to have access to the blurry image  $b$ , formed from the sharp image  $x$  in Fig. 1, but since we only have access to  $y$ , this approach should rather be applied on a demosaicked version  $d$  of  $y$  approximating  $b$ .

The raw image formation model of Eq. (1) is particularly well-suited for camera PSF removal since the properties of most recent lenses are accurately measured and tabulated<sup>1</sup> or can be estimated with calibration of a camera, *e.g.*, [11, 28], or with an optimization-based technique, *e.g.*, [29, 34]. This ensures that  $K$  is known for this task. The mosaicking pattern in  $M$  is a feature of the camera and can reasonably be supposed known too in general.

<sup>1</sup><https://www.dxomark.com/Lenses/>

## 4 Proposed approach

A natural approach for solving a joint deblurring, demosaicking and denoising problem is to leverage the important previous work on image demosaicking and denoising and non-blind RGB image deblurring by using a two-stage method stacking a joint demosaicking and denoising solver followed by a non-blind deblurring approach, *e.g.*, [28], as shown in Figure 1. One of the main contributions of this work is to instead predict a sharp, demosaicked and denoised image from the observation  $y$ .

### 4.1 Energy function and splitting strategies

We integrate the forward model (1) into a penalized energy function with an image prior  $\Omega$  whose solution is a denoised and deblurred linRGB image:

$$\min_x \frac{1}{2} \|y - MKx\|_F^2 + \lambda\Omega(x). \quad (2)$$

Optimization of (2) is traditionally carried out with splitting algorithms such as half-quadratic splitting (or HQS) [8]. We introduce an auxiliary variable  $z$  and solve

$$\min_{x,z} \frac{1}{2} \|y - MKz\|_F^2 + \lambda\Omega(x) \quad s.t. \quad z = x, \quad (3)$$

which becomes, when relaxed with a weight  $\beta > 0$ :

$$\min_{x,z} \frac{1}{2} \|y - MKz\|_F^2 + \frac{\beta}{2} \|z - x\|_F^2 + \lambda\Omega(x). \quad (4)$$

Optimization requires to jointly handle the operators  $M$  and  $K$ . We will detail the calculations in the next paragraphs.

Alternatively, we first demosaick the image, for instance with a CNN  $\xi$  with parameter  $\nu$  [9], and second use a non-blind deblurring approach on the demosaicked linRGB image to predict the final sharp linRGB image  $x$ . The same relaxation of a constraint on an auxiliary variable  $z$  leads to

$$\begin{aligned} \min_{x,z} \frac{1}{2} \|d - Kz\|_F^2 + \frac{\beta}{2} \|z - x\|_F^2 + \lambda\Omega(x), \\ \text{with } d = \xi_\nu(y, \lambda_r, \lambda_s). \end{aligned} \quad (5)$$

The demosaicking approach takes as input the noise parameters  $\lambda_r$  and  $\lambda_s$ , in the vein of [9, 14]. In this case, the reference image in the non-blind deblurring problem is  $d$  and not  $y$ .

### 4.2 Solving the intermediate problems

Predicting  $x$  in both Eqs (4) and (5) is done by solving

$$\min_x \lambda\Omega(x) + \frac{\beta}{2} \|z - x\|_F^2. \quad (6)$$

The minimizer of energy can be computed by evaluating in  $z$  the proximal operator  $\phi$  of  $\Omega$  with parameter  $\lambda/\beta$  [23]:

$$x = \text{prox}_\Omega(z, \lambda/\beta) = \phi(z, \lambda/\beta). \quad (7)$$

The intermediate deblurred image in (5) is the solution of:

$$\min_z \|d - Kz\|_F^2 + \beta \|z - x\|_F^2, \quad (8)$$

which is classically solved with fast Fourier transform (FFT) [35], conjugate gradient (CG) [25], or Richardson fixed point iterations [6].

However estimating  $z$  in Eq. (4) requires solving instead:

$$\min_z \|y - MKz\|_F^2 + \beta \|z - x\|_F^2, \quad (9)$$

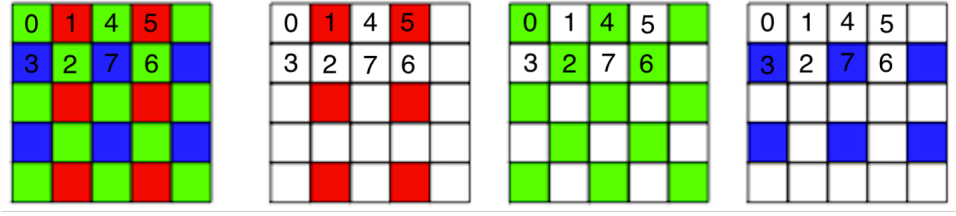


Figure 2: A mosaicked image with the Bayer pattern and its three sampled colored components.

For any mosaicking pattern choice,  $M$  independently samples the color channels resulting in

$$MKz = \begin{bmatrix} D_R K_R & 0 & 0 \\ 0 & D_G K_G & 0 \\ 0 & 0 & D_B K_B \end{bmatrix} \begin{bmatrix} z_R \\ z_G \\ z_B \end{bmatrix} \quad (10)$$

where  $z_R$ ,  $z_G$  and  $z_B$  are the red, green and blue components and  $K_R$ ,  $K_G$  and  $K_B$  are the color-specific components of the blur  $K$ . One of our contributions is to estimate  $z_R^*$ ,  $z_G^*$  and  $z_B^*$ , the red, green and blue images forming  $z^*$ , the solution of (9), with a FFT-based module similar to the one of [35] in the case of the Bayer pattern.

### 4.3 FFT-based solver for least-squares (9)

We solve Eq. (9) with a FFT-based module inspired by [35] in the context of image upsampling. The linear operator  $MK$  in (10) decomposes the least-squares problem Eq. (9) into three independent terms. Figure 2 shows a mosaicked image  $y$  obtained sampled with  $M$  and whose  $y_R$  and  $y_B$  components are sampled versions of the corresponding RGB image where in each  $2 \times 2$  non-overlapping patch, only one pixel value is retained per color. Similarly, the  $y_G$  is the sum of two images  $y_{G_1}$  and  $y_{G_2}$  such that  $y_G = y_{G_1} + y_{G_2}$  (and  $D_G = D_{G_1} + D_{G_2}$ ), each one sampling a single green pixel in the  $2 \times 2$  non-overlapping patches in Fig. 2. We interpolate the missing values by solving, with  $c$  in  $\{G_1, R, G_2, B\}$ :

$$\min_{z_c} \|y_c - D_c K_c z_c\|_F^2 + \beta \|z_c - x_c\|_F^2. \quad (11)$$

These four problems are similar to the upsampling approach of [35] with rate 2 solving the linear system, with  $c$  in  $\{G_1, R, G_2, B\}$ :

$$(K_c^\top D_c^\top D_c K_c + \beta I) z_c^* = K_c^\top D_c^\top y + \beta x_c. \quad (12)$$

By splitting the green image into  $y_{G_1}$  and  $y_{G_2}$ , we efficiently solve the four least-squares with an adapted version of the FFT-based approach of [35, 36]. We detail the implementation details and modifications on the code of [35] in the supplemental material. The images  $z_R^*$  and  $z_B^*$  are the solutions of (12) and  $z_G^*$  is obtained from  $z_{G_1}^*$  and  $z_{G_2}^*$  as follows: the pixels at locations 0, 4, ... (resp. 2, 6, ...) in Fig. 2 are copied from the ones from  $z_{G_1}^*$  (resp.  $z_{G_2}^*$ ) and the remaining pixels at locations 1, 3, 5, ... are the corresponding values in  $(z_{G_1}^* + z_{G_2}^*)/2$ . Stacking the three images  $z_R^*$ ,  $z_G^*$  and  $z_B^*$  yields the RGB solution  $z^*$  of Eq. (9).

### 4.4 Learnable embedding

We improve the performance of the restoration method for solving either (5) or (4), we embed a few stages of HQS in the USRNet model of Zhang *et al.*, [35] featuring two modules for learning the proximal step (6) and estimating on-the-fly the optimal weights  $\beta^{(t)}$  and  $\gamma^{(t)} = \lambda/\beta^{(t)}$  ( $t = 1, \dots, T$ ). We parameterize the proximal operator of  $\phi$  with the same Unet model as in [35] with parameter  $\theta$  such that for a given estimate  $z^{(t)}$ , we predict an RGB image  $x$  as

$$x^{(t+1)} = \phi_\theta(z^{(t)}, \gamma^{(t+1)}). \quad (13)$$

We predict  $z^{(t+1)}$  from  $x^{(t+1)}$ ,  $K$ ,  $M$  and  $\beta^{(t+1)}$  with the mapping  $\psi$  estimating its  $R$ ,  $G$  and  $B$  components with the approach of Section 4.3:

$$z^{(t+1)} = \psi(x^{(t+1)}, K, M, \beta^{(t+1)}), \quad (14)$$

---

**Algorithm 1:** Parametric function for solving (4).

---

**Data:**  $y, K, M, \lambda_r, \lambda_s, \theta, \omega$   
// Weights prediction  
1  $[\{\beta^{(t)}\}_{t=1}^T, \{\gamma^{(t)}\}_{t=1}^T] = \chi_\omega(\lambda_r, \lambda_s);$   
// Demosaicking  
2  $d \leftarrow \xi_\nu(y, \lambda_r, \lambda_s);$   
3  $t \leftarrow 1;$   
4  $x \leftarrow d;$   
// Restoration with variant of [35]  
5 **for**  $t \leq T$  **do**  
6      $z \leftarrow \psi(y, x, K, M, \beta^{(t)});$   
7      $x \leftarrow \phi_\theta(z, \gamma^{(t)});$   
8      $t \leftarrow t + 1;$   
9 **end**  
**Result:** Restored linRGB image  $x$ .

---

---

**Algorithm 2:** Parametric function for solving (5).

---

**Data:**  $y, K, \lambda_r, \lambda_s, \theta, \omega, \nu$   
// Weights prediction  
1  $[\{\beta^{(t)}\}_{t=1}^T, \{\gamma^{(t)}\}_{t=1}^T] = \chi_\omega(\lambda_r, \lambda_s);$   
// Demosaicking  
2  $d \leftarrow \xi_\nu(y, \lambda_r, \lambda_s);$   
3  $t \leftarrow 1;$   
4  $x \leftarrow d;$   
// Deblurring with [35]  
5 **for**  $t \leq T$  **do**  
6      $z \leftarrow \psi(d, x, K, I, \beta^{(t)});$   
7      $x \leftarrow \phi_\theta(z, \gamma^{(t)});$   
8      $t \leftarrow t + 1;$   
9 **end**  
**Result:** Restored s/linRGB image  $x$ .

---

where  $x^{(t+1)}$ ,  $K$ ,  $M$  and  $\beta^{(t+1)}$  are used to build the least-squares problems (12). The weights  $\beta^{(t)}$  and  $\gamma^{(t)}$  with a 3-layer perceptron, as detailed in [35] dubbed  $\chi$  and with parameter  $\omega$ . In our case, it becomes a function of the read and shot noise coefficients  $\lambda_r$  and  $\lambda_s$  defined as:

$$[\{\beta^{(t)}\}_{t=1}^T, \{\gamma^{(t)}\}_{t=1}^T] = \chi_\omega(\lambda_r, \lambda_s). \quad (15)$$

Our proposed approach for joint deblurring, demosaicking and denoising of raw images embeds the weight predictor  $\chi_\omega$ , the learnable proximal operator  $\phi_\theta$  and the FFT-based solver for joint deblurring and demosaicking  $\psi$  in (14) into the state-of-the-art model USRNet [35] initially designed for sRGB image non-blind deblurring and upsampling.

The two-stage approach first jointly demosaicks and denoises a raw image with a module  $\xi_\nu$  that we implement with the learning-free approach of [20] or the state-of-the-art approach of [9] dubbed Deepjoint. It is followed by a non-blind deblurring module that we implement with the USRNet model of [35]. We modify Deepjoint and USRNet for processing the noise parameters  $\lambda_s$  and  $\lambda_r$  in place of the variance of a traditional Gaussian noise model. These two approaches are summarized in Algorithms 1 and 2. The main difference is that in Alg. 1, our approach takes  $y$  as reference during inference whereas Alg. 2 uses  $y$  only in the joint demosaicking and denoising module. In this case, the deblurring module could predict wrong details as it takes the demosaicked image  $d$  which might contain prediction errors such as Moiré artifacts.

## 5 Experiments

We run the experiments on an NVIDIA Tesla V100 graphic card. The code will be made available if the paper is accepted.

**Experimental setting.** We extract  $96 \times 96$  patches in the training images of DIV2K and Flickr2K datasets, often used for training image upsampling models and featuring high-resolution edges, Moiré artifacts-prone textures and little compression artifacts. We convert these patches into the linRGB format with the pipeline of [3], blur them with uniform blur from [35] and add affine noise generated with the code of [3]. We randomly flip and rotate the patches as augmentation. We extract 5000 patches from the 100 images of DIV2K validation set to form ours. Since blur is color-dependent [28, 29, 34], we synthesize RGB blur kernels (details in what follows) that are more realistic than grayscale filters such as the ones of [17]. We use Adam optimizer with initial learning rate set to  $10^{-4}$ . The learning rate is divided by 2 whenever the validation loss plateaus during 15 epochs until reaching  $10^{-6}$ . We use a batch size of 32. We use the  $\ell_1$  loss to compare the ground-truth patches and the predictions in the sRGB format as done in [3].

**Generating color-specific blur kernels.** Real blurs are color-specific because of the diffraction effect of a lens. This can be seen on the PSFs estimated by [28], which locally is modelled with an RGB uniform kernel whose components are smoothly varying across color channels [28, 34]. We thus build RGB kernels for training, validating and testing the models in a more realistic setting than traditional Levin’s kernels [17] for instance. We generate a  $25 \times 25$  grayscale kernels with the code of Zhang *et al.*, [35] representing both motion and anisotropic Gaussian blurs. This synthetic kernel is arbitrarily set as the blue

Datasets Noise level Color space	Kodak (192 images)				Sun (640 images)			
	Noiseless		With noise		Noiseless		With noise	
	linRGB	sRGB	linRGB	sRGB	linRGB	sRGB	linRGB	sRGB
[20] + [15]	33.15/0.91	28.03/0.78	30.94/0.79	22.77/0.47	36.55/0.93	29.99/0.82	32.57/0.79	23.59/0.50
[20] + [35] (s/s)	- / -	32.16/0.88	- / -	29.56/0.78	- / -	33.50/0.91	- / -	30.40/0.80
[20] + [35] (lin/lin)	<u>35.92/0.94</u>	31.92/0.89	<u>33.74/0.90</u>	29.42/0.78	<u>39.43/0.96</u>	33.77/0.91	36.27/0.92	30.46/0.81
[20] + [35] (lin/s)	<u>35.28/0.95</u>	32.28/0.90	<u>33.28/0.90</u>	<u>29.69/0.79</u>	<u>38.73/0.96</u>	34.21/0.92	<b>35.83/0.92</b>	<u>30.66/0.81</u>
[9] + [15]	32.85/0.90	27.89/0.75	32.10/0.87	26.87/0.69	36.07/0.92	29.69/0.80	34.92/0.90	28.26/0.73
[9] + [35] (s/s)	- / -	30.27/0.83	- / -	29.01/0.77	- / -	31.73/0.86	- / -	30.07/0.80
[9] + [35] (lin/lin)	<u>35.83/0.94</u>	31.67/0.88	<u>33.88/0.90</u>	<u>29.48/0.79</u>	<u>38.97/0.96</u>	33.24/0.90	<u>36.11/0.92</u>	<u>30.35/0.81</u>
[9] + [35] (lin/s)	<u>35.04/0.94</u>	32.12/0.88	<u>33.12/0.90</u>	<u>29.61/0.78</u>	<u>37.98/0.96</u>	33.61/0.90	<u>35.54/0.91</u>	<u>30.58/0.81</u>
Ours (lin/lin)	<b>36.48/0.95</b>	<u>32.46/0.90</u>	<b>34.10/0.91</b>	<b>29.76/0.80</b>	<b>40.10/0.97</b>	<u>34.39/0.93</u>	<b>36.51/0.92</b>	<b>30.72/0.82</b>
Ours (lin/s)	<u>35.72/0.95</u>	<u>32.99/0.91</u>	<u>33.52/0.91</u>	<u>29.98/0.80</u>	<u>39.13/0.97</u>	<u>34.90/0.93</u>	<u>35.93/0.92</u>	<u>30.86/0.82</u>
Ours (lin/s, gray)	<u>35.08/0.94</u>	32.21/0.89	<u>33.26/0.90</u>	<u>29.72/0.79</u>	<u>38.48/0.96</u>	34.15/0.92	<u>35.81/0.92</u>	<b>30.71/0.82</b>
Ours (lin/s, [9])	<u>35.86/0.95</u>	<b>33.37/0.92</b>	<u>33.53/0.91</u>	<b>30.14/0.80</b>	<u>39.21/0.97</u>	<b>35.19/0.94</b>	<u>35.87/0.92</u>	<b>30.95/0.82</b>

Table 1: Joint deblurring, denoising and demosaicking comparison. Best result is in bold font. Second best is underlined.

component. The other ones are randomly rotated versions with small angles in  $[-5^\circ, +5^\circ]$  and rescaled by a factor  $[0.8, 1]$ . This yields a  $25 \times 25 \times 3$  array.

**Joint deblurring, denoising and demosaicking.** We evaluate our method on two synthetic datasets. We convert the 24 and 80 images of the Kodak [18] and Sun [31] datasets into linRGB images with the pipeline of [3] and blur them with the 8 filters of [17] we transform into RGB kernels. We add noise with the code of [3] with  $\log(\lambda_s)$  chosen in  $[10^4, 3 \times 10^{-3}]$  and corresponding  $\lambda_r$  in the model of [3], *i.e.*, small to moderate noise, and mosaick them to form respectively 192 and 640 test samples. We compare our approach on raw images with two-stage methods. For demosaicking, we use either the filtering approach of [20] or the CNN for joint demosaicking and denoising of [9]. We retrain [9] to take into account the noise distribution of [3] on the 2.5 million patches of [9]. For non-blind deblurring, we use [15] based on a hyper-Laplacian image prior or the unrolled model of [35]. We retrain [35] each time on the images predicted by the first stage implemented with [9] or [20] to take into account prediction errors. As we predict linRGB images but ultimately want enhanced sRGB images, we compare three kinds of supervision: (i) the intermediate image  $d$  is converted into an sRGB image and [35] is supervised with sRGB targets (s/s), (ii) [35] deblurs a linRGB demosaicked image and is supervised with linRGB targets (lin/lin), and (iii) [35] deblurs a linRGB demosaicked image and is supervised with sRGB targets as in [3] (lin/s). We train a variant of our model in the “lin/lin” setting and three in the “lin/s” setting: one with initial guess demosaicked with simple bilinear interpolation, one with initial guess obtained with [9] (lin,s [9]) and one trained with grayscale kernels only (lin/s, gray). We unroll  $T = 6$  iterations of HQS in the different implementations of [35] in Algorithms (1) and (2) implemented by the baselines and our approach.

Table 1 shows the PSNR and SSIM scores on the images after we crop 50 pixels on the borders to discard any boundary artifact in the measurements. Our methods achieve on the four sets the best PSNR/SSIM score by PSNR margins of 0.5dB and SSIM margins of 0.01 or 0.02 over the two-stage methods. Methods trained with supervision on linRGB images naturally have the best scores on this color format but are behind the other methods in the sRGB format, suggesting supervision with sRGB sharp images with the approach of [3] is also beneficial for deblurring and demosaicking raw degraded images. Our variant trained only on grayscale kernels is in the ballpark of the best ones in the noisy cases but lags behind them by margins of 1dB in the noiseless case, meaning it cannot restore as fine details as the methods trained with the same blur distribution. The table also shows that initialization matters as the method with initial guess produced by [9] leads to better results, with margins ranging from 0.1 to 0.4dB on sRGB images, compared to the one initialized with a demosaicked image bilinearly interpolated. Figure 3 shows two restoration examples of blurry, mosaicked and noisy raw images (displayed as sRGB images) obtained with our best performing method and the best performer from the two-stage techniques. We also provide comparison with the same images but with the classical grayscale kernels of [17] in the supplemental material. The method is as fast as vanilla USRNet [35] since the only modification that might alter running time is the FFT-based module whose computation time is negligible compared to evaluating a CNN. It takes about 1 second to process a 720p image and at most 5 seconds for a 2K image.





Figure 3: Examples of jointly deblurred, demosaicked and denoised images. We show the degraded raw images in the sRGB format. Compared to the two-stage method [20]+ [35], our method restores finer details.



Figure 4: Restored examples with a  $65 \times 65$  blur kernel and noise parameters set to  $\lambda_s = 10^{-3}$  and  $\lambda_r = 1.3 \times 10^{-6}$ . Better seen on a computer screen. Both quantitatively and visually our method outperforms the two-stage method [9]+ [35].

**Robustness to larger kernels.** We train the different models with  $25 \times 25$  kernels but we show in Fig. 4 that our method can be used with much larger filters. The image is blurred with a  $65 \times 65$  kernel from [22]. We compare the two-stage strategy [9]+ [35] to ours, both trained with the “lin/lin” setting. Our method achieves a better PSNR score and visual aspect compared to the two-stage method. This is typical of our observations on other large kernels from [22].

**Camera PSF removal.** We now remove the aberrations of a consumer-grade lens PSF. We restore the blurry image<sup>2</sup> shot with a Canon Mark II reflex camera and a canon 24mm f/1.4 lens at maximal aperture and whose PSF has been measured by two approaches<sup>3</sup>: a calibration method [28] and a variational approach [29].

We convert the corresponding sRGB real blurry image into a raw image with the camera pipeline of [3]. We follow [28,29] and break the full image into overlapping patches where the PSF boils down to a locally uniform blur kernel. We restore each patch with our model trained for the previous experiment without fine-tuning it with the PSF, stitch them together as detailed in [28] and convert the restored image back into the sRGB format. We show in Figure 5 the results for the PSF obtained with camera calibration (PSF1) and the one predicted with a variational method (PSF2). We compare them to the image restored in [28] that also removes blur from the raw image provided with the PSFs. Our methods can restore finer details such as the words on the panels or the closest in Figure 5, with both PSFs. We provide other examples of PSF removal from real images shot with the same lens in the supplemental material.

We also produce quantitative results on synthetic data in Table 2. Since there is no existing pairs of blurry and sharp images from modern SLRs, we collect the 53 images with ratio height/width of 2/3 from the DIV2K validation dataset matching the

<sup>2</sup><https://www.webdav.tuebingen.mpg.de/pixel/lenscorrection/>

<sup>3</sup>[https://www.webdav.tuebingen.mpg.de/pixel/blind\\_lenscorrection/](https://www.webdav.tuebingen.mpg.de/pixel/blind_lenscorrection/)





Figure 5: The real blurry image of [28] was taken with a modern digital SLR and a zoom lens at maximal aperture, exhibiting chromatic aberrations, especially on the corners where the lens is the most curved. Our method efficiently removes the blur caused by the optics, provided either a calibrated or an approximate PSF (best seen on a computer screen).

PSFs	GT [28]		Approx. [29]	
	linRGB	sRGB	linRGB	sRGB
[20]+ [35]	41.22	35.22	<b>36.20</b>	<b>29.87</b>
[9]+ [35]	40.86	35.04	35.72	29.50
Ours	41.14	<u>35.77</u>	35.53	29.28
Ours (gray)	<b>41.40</b>	35.63	<u>36.13</u>	<u>29.76</u>
Ours ( [9])	<u>41.34</u>	<b>35.84</b>	35.47	29.21

Table 2: PSF removal comparison.

ratio of the PSFs measured by [28, 29]. We convert them into linRGB images with [3], blur them with the PSF obtained by calibration of the camera in [28] (which thus becomes the *ground-truth* blur for the synthetic data), mosaick them and finally add affine noise with the same parameters as in previous experiment. We evaluate the methods from Tab. 1 trained in the (lin/s) setting *without* further retraining them on the PSFs of [28, 29]. We restore the images with the PSF from [28] used to generate the blurry images and dubbed “GT” in Tab. 2 and the one from [29], considered as an approximate blur we call “Approx.” in Tab. 2.

We achieve the best PSNR score with the “GT” PSF used to build the synthetic images with margins of +0.6dB on the two-stage methods and a margin of 0.2dB over the variant trained uniquely on grayscale kernels. However the two-stage techniques achieve better results with the “Approx.” PSF by a margin of 0.6dB over our methods trained on RGB kernels and a small margin of less than 0.1dB over our method trained on grayscale kernels. It suggests that our synthetic RGB kernels help to improve the performance of our joint restoration model when the PSF is accurately known. This is a reasonable assumption provided professional lens benchmarks. However the drop of performance with approximate kernels could be explained by our model overfitting colored filters that might not have a realistic distribution permitting robustness to large prediction errors in the blur. On the one hand, we could be able to improve results on approximate blurs in Tab. 2 with more realistic models of RGB kernels but on the other hand, the example in Figure 5 shows that our method can already handle predicted blurs in real-world scenarios.

## 6 Conclusion

We have presented a approximate forward model for joint deblurring, demosaicking and denoising images, derived from a digital camera pipeline. We have proposed a penalized energy based on it, solved with HQS. Iterations of this method are embedded into a parametric function inspired by [35], restoring raw images and supervised with the technique of [3]. Our experiments have shown that it outperforms two-stage approaches, decomposing the problem into a demosaicking step

followed by non-blind deblurring, quantitatively and visually and in the presence of affine noise. Our approach have been applied to the removal of chromatic aberrations caused by the optics of a camera from real images, when the PSF is estimated beforehand. Future work includes the generation of more realistic training data, such as blur kernels, to remove more optical aberrations, *e.g.*, coma, from raw images.

**Acknowledgments:** This work was funded in part by the French government under management of Agence Nationale de la Recherche as part of the "Investissements d'avenir" program, reference ANR-19-P3IA-0001 (PRAIRIE 3IA Institute), the Louis Vuitton/ENS Chair in Artificial Intelligence and the Inria/NYU collaboration. Jian Sun was supported by NSFC (11971373, U20B2075, 12026605).

## References

- [1] Abdelrahman Abdelhamed, Marcus Brubaker, and Michael S. Brown. Noise flow: Noise modeling with conditional normalizing flows. In *Proceedings of the International Conference on Computer Vision (ICCV)*, pages 3165–3173, 2019.
- [2] Abdelrahman Abdelhamed, Stephen Lin, and Michael S. Brown. A high-quality denoising dataset for smartphone cameras. In *Proceedings of the Conference on Computer Vision and Pattern Recognition (CVPR)*, pages 1692–1700, 2018.
- [3] Tim Brooks, Ben Mildenhall, Tianfan Xue, Jiawen Chen, Dillon Sharlet, and Jonathan T. Barron. Unprocessing images for learned raw denoising. In *Proceedings of the Conference on Computer Vision and Pattern Recognition (CVPR)*, pages 11036–11045, 2019.
- [4] Yunjin Chen and Thomas Pock. Trainable nonlinear reaction diffusion: A flexible framework for fast and effective image restoration. *IEEE Transactions on Pattern Analysis and Machine Intelligence (TPAMI)*, 39(6):1256–1272, 2017.
- [5] Jiangxin Dong, Stefan Roth, and Bernt Schiele. Deep wiener deconvolution: Wiener meets deep learning for image deblurring. In *Advances in Neural Information Processing Systems (NeurIPS)*, 2020.
- [6] Thomas Eboli, Jian Sun, and Jean Ponce. End-to-end interpretable learning of non-blind image deblurring. In *Proceedings of the European Conference on Computer Vision (ECCV)*, pages 314–331, 2020.
- [7] Alessandro Foi, Mejdi Trimeche, Vladimir Katkovnik, and Karen O. Egiazarian. Practical poissonian-gaussian noise modeling and fitting for single-image raw-data. *IEEE Transactions on Image Processing (TIP)*, 17(10):1737–1754, 2008.
- [8] Donald Geman and George Reynolds. Constrained restoration and the recovery of discontinuities. *IEEE Transactions on Pattern Analysis and Machine Intelligence (TPAMI)*, 14(3):367–383, 1992.
- [9] Michaël Gharbi, Gaurav Chaurasia, Sylvain Paris, and Frédo Durand. Deep joint demosaicking and denoising. *ACM Transactions on Graphics (ToG)*, 35(6):191:1–191:12, 2016.
- [10] Rafael. C. Gonzalez and Richard. E. Woods. *Digital Image Processing*. Addison-Wesley Publishing Company, Inc., 1992.
- [11] Eric Kee, Sylvain Paris, Simon Chen, and Jue Wang. Modeling and removing spatially-varying optical blur. In *Proceedings of the International Conference on Computational Photography (ICCP)*, pages 1–8, 2011.
- [12] Daniel Khashabi, Sebastian Nowozin, Jeremy Jancsary, and Andrew W. Fitzgibbon. Joint demosaicing and denoising via learned nonparametric random fields. *IEEE Transactions on Image Processing (TIP)*, 23(12):4968–4981, 2014.
- [13] Teresa Klatzer, Kerstin Hammernik, Patrick Knöbelreiter, and Thomas Pock. Learning joint demosaicing and denoising based on sequential energy minimization. In *Proceedings of the International Conference on Computational Photography (ICCP)*, pages 1–11, 2016.
- [14] Filippas Kokkinos and Stamatios Lefkimmiatis. Iterative joint image demosaicking and denoising using a residual denoising network. *IEEE Transactions on Image Processing (TIP)*, 28(8):4177–4188, 2019.
- [15] Dilip Krishnan and Rob Fergus. Fast image deconvolution using hyper-laplacian priors. In *Advances in Neural Information Processing Systems (NeurIPS)*, pages 1033–1041, 2009.
- [16] Jakob Kruse, Carsten Rother, and Uwe Schmidt. Learning to push the limits of efficient fft-based image deconvolution. In *Proceedings of the International Conference on Computer Vision (ICCV)*, pages 4596–4604, 2017.
- [17] Anat Levin, Yair Weiss, Frédo Durand, and William T. Freeman. Understanding and evaluating blind deconvolution algorithms. In *Proceedings of the Conference on Computer Vision and Pattern Recognition (CVPR)*, pages 1964–1971, 2009.
- [18] Xin Li, Bahadır Gunturk, and Lei Zhang. Image demosaicing: a systematic survey. In *Visual Communications and Image Processing*, volume 6822, pages 489 – 503, 2008.
- [19] Chih-Hung Liang, Yu-An Chen, Yueh-Cheng Liu, and Winston H. Hsu. Raw image deblurring. *Technical report*, arXiv:2012.04264, 2020.
- [20] Daniele Menon, Stefano Andriani, and Giancarlo Calvagno. Demosaicing with directional filtering and a posteriori decision. *IEEE Transactions on Image Processing (TIP)*, 16(1):132–141, 2007.
- [21] Seungjun Nah, Tae Hyun Kim, and Kyoung Mu Lee. Deep multi-scale convolutional neural network for dynamic scene deblurring. In *Proceedings of the Conference on Computer Vision and Pattern Recognition (CVPR)*, pages 257–265, 2017.

- [22] Jinshan Pan, Deqing Sun, Hanspeter Pfister, and Ming-Hsuan Yang. Deblurring images via dark channel prior. *IEEE Transactions on Pattern Analysis and Machine Intelligence (TPAMI)*, 40(10):2315–2328, 2018.
- [23] Neal Parikh and Stephen P. Boyd. Proximal algorithms. *Foundations and Trends on Optimization*, 1(3):127–239, 2014.
- [24] Tobias Plotz and Stefan Roth. Benchmarking denoising algorithms with real photographs. In *Proceedings of the Conference on Computer Vision and Pattern Recognition (CVPR)*, pages 2750–2759, 2017.
- [25] Kari Pulli. Flexisp: a flexible camera image processing framework. *ACM Transactions on Graphics (ToG)*, 33(6):231:1–231:13, 2014.
- [26] Uwe Schmidt, Carsten Rother, Sebastian Nowozin, Jeremy Jancsary, and Stefan Roth. Discriminative non-blind deblurring. In *Proceedings of the Conference on Computer Vision and Pattern Recognition (CVPR)*, pages 604–611, 2013.
- [27] Christian J. Schuler, Harold Christopher Burger, Stefan Harmeling, and Bernhard Schölkopf. A machine learning approach for non-blind image deconvolution. In *Proceedings of the Conference on Computer Vision and Pattern Recognition (CVPR)*, pages 1067–1074, 2013.
- [28] Christian J. Schuler, Michael Hirsch, Stefan Harmeling, and Bernhard Schölkopf. Non-stationary correction of optical aberrations. In *Proceedings of the International Conference on Computer Vision (ICCV)*, pages 659–666, 2011.
- [29] Christian J. Schuler, Michael Hirsch, Stefan Harmeling, and Bernhard Schölkopf. Blind correction of optical aberrations. In *Proceedings of the European Conference on Computer Vision (ECCV)*, pages 187–200, 2012.
- [30] Ferréol Soulez and Éric Thiébaud. Joint deconvolution and demosaicing. In *Proceedings of the International Conference on Image Processing (ICIP)*, pages 145–148, 2009.
- [31] Libin Sun, Sunghyun Cho, Jue Wang, and James Hays. Edge-based blur kernel estimation using patch priors. In *Proceedings of the International Conference on Computational Photography (ICCP)*, pages 1–8, 2013.
- [32] Xin Tao, Hongyun Gao, Xiaoyong Shen, Jue Wang, and Jiaya Jia. Scale-recurrent network for deep image deblurring. In *Proceedings of the Conference on Computer Vision and Pattern Recognition (CVPR)*, pages 8174–8182, 2018.
- [33] Mejdí Trimeche, Dmitriy Paliy, Markku Vehvilainen, and Vladimir Katkovnik. Multichannel image deblurring of raw color components. In *Computational Imaging*, volume 5674, pages 169–178, 2005.
- [34] Tao Yue, Jin-Li Suo, Jue Wang, Xun Cao, and Qionghai Dai. Blind optical aberration correction by exploring geometric and visual priors. In *Proceedings of the Conference on Computer Vision and Pattern Recognition (CVPR)*, pages 1684–1692, 2015.
- [35] Kai Zhang, Luc Van Gool, and Radu Timofte. Deep unfolding network for image super-resolution. In *Proceedings of the Conference on Computer Vision and Pattern Recognition (CVPR)*, pages 3214–3223, 2020.
- [36] Ningning Zhao, Qi Wei, Adrian Basarab, Nicolas Dobigeon, Denis Kouame, and Jean-Yves Tournet. Fast single image super-resolution using a new analytical solution for  $\ell_2$ - $\ell_2$  problems. *IEEE Transactions on Image Processing (TIP)*, 25(8):3683–3697, 2016.
- [37] Daniel Zoran and Yair Weiss. From learning models of natural image patches to whole image restoration. In *Proceedings of the International Conference on Computer Vision (ICCV)*, pages 479–486, 2011.